The triple junction hull: Tools for grain boundary network design

The Triple Junction Hull: Tools For Grain Boundary Network Design

Oliver K. Johnson[a,*], Christopher A. Schuh[a]

[a]*Department of Materials Science and Engineering, Massachusetts Institute of Technology, 77 Massachusetts Ave., Cambridge MA 02139, USA*

Abstract

Grain boundary engineering (GBE) studies have demonstrated significant materials properties enhancements by modifying the populations and connectivity of different types of grain boundaries within the grain boundary network. In order to facilitate rigorous design and optimization of grain boundary networks, we develop theoretical tools that are based upon a spectral representation of grain boundary network statistics. We identify the connection between a local length scale, embodied by triple junctions, and a global length scale, associated with the grain boundary network configuration as a whole. We define the local state space for triple junctions, $\mathscr{A}^{(3)}$, and enumerate its symmetries. We further define the design space for grain boundary networks, $\mathscr{M}_H^{(3)}$, characterize its important geometric properties, and discuss how its convexity permits grain boundary network design. We also investigate the extent to which the control of texture alone allows one to probe the full design space.

Keywords: Triple Junctions, TJDF, Microstructure Design, Grain Boundary Network, Grain Boundary Engineering

1. Introduction

In the context of texture and grain structure in polycrystalline materials, microstructure design tools now allow the designer to explore a complete set of physically realizable microstructures and identify those that meet various performance objectives and design constraints (Adams et al., 2001, 2012). These tools have been used to address design problems in which elastic and plastic properties are concerned (Adams et al., 2001; Fast et al., 2008; Houskamp et al., 2007; Kalidindi and Houskamp, 2007; Kalidindi et al., 2004; Lyon and Adams, 2004; Saheli et al., 2005; Sintay and Adams, 2005). However, their application to other properties of scientific and engineering interest, such as fracture and corrosion, which depend upon the structure of the grain boundary network, remains to be addressed. This is an area of great opportunity because grain boundary engineering (GBE) studies have demonstrated significant enhancements of materials properties (Lehockey et al., 1999; Lehockey and Palumbo, 1997; Lehockey et al., 1998a,b; Norton et al., 1996), but

*Corresponding Author: Tel. +1-617-258-5547

Email addresses: ojohnson@mit.edu (Oliver K. Johnson), schuh@mit.edu (Christopher A. Schuh)

there is currently no "inductive" method (Olson, 1997) by which to design such successes *a priori*. For instance, Lin et al. observed a two-fold decrease in the intergranular corrosion rate of Alloy 600 after GBE processing (Lin et al., 1995). However, no major change in texture accompanied this enhancement in properties. Characteristic of GBE materials, the resultant texture was nearly random, but contained a high fraction of low-energy grain boundaries (up to 55% of the boundaries were $\Sigma 3$ type). Contrast this with the fact that for a microstructure with uncorrelated grain orientations and random texture the expected population of such boundaries is extremely small ($\sim$1.8%) (Morawiec et al., 1993). It would appear, then, that texture is insufficient to explain or predict such materials properties enhancements and, consequently, design tools that incorporate the character and connectivity of the grain boundary network are needed.

In previous work, we introduced a general triple junction distribution function (TJDF) as the core of a design strategy for grain boundary networks (Johnson and Schuh, 2013). The TJDF provides a statistical description of grain boundary network connectivity that facilitates adaptation of the existing design framework to grain boundary network design. Expressed in the context of the spectral framework of Johnson and Schuh (2013), the TJDF provides a bridge between crystallographic texture and grain boundary network topology. These tools allow one to rigorously bound the universe of all possible grain boundary network configurations. In this work, we employ our previous results in order to define the triple junction hull, $\mathscr{M}_H^{(3)}$, which constitutes the first order design space for grain boundary networks. $\mathscr{M}_H^{(3)}$ bounds the entire space of physically realizable grain boundary networks, and is pivotal for the adaptation of existing tools to the problem of grain boundary network design. We also investigate the relative size of the subspace of $\mathscr{M}_H^{(3)}$ that is accessible through the control of crystallographic texture alone.

2. Triple Junction State Space

Grain boundary network design is an intrinsically multi-scale endeavor, requiring the practitioner to specify both (1) the local state and (2) the spatial location of grain boundaries within the network. However, real grain boundary networks exhibit local correlations that dominate at the length scale of triple junctions (Frary and Schuh, 2005) and encode network connectivity information. This suggests that the most convenient unit for grain boundary network design is, in fact, the triple junction.

Figs. 1a and 1b illustrate the two dominant length scales that must be considered in the design of grain boundary networks: that of the triple junction (*i.e.* the characteristic length scale of network connectivity), and that of the network as a whole. The duplicity of length scales in the physical grain boundary network is also reflected in the design space, which encompasses both the local state space of the triple junctions, and the global configuration space of the network. We will begin by defining the local state space for triple junctions, and in the subsequent section we will address the configuration space of the network as a whole.

A triple junction is the one-dimensional edge common to three adjacent grains, or, equivalently, the one-dimensional intersection of three grain boundaries. It is geometrically defined by eleven macroscopic state parameters. Five of these define the inclinations of the incident grain boundary planes. The other six characterize the lattice misorientations between pairs of grains adjoining each of the three intersecting grain boundaries, and it is on these that we will concentrate in this

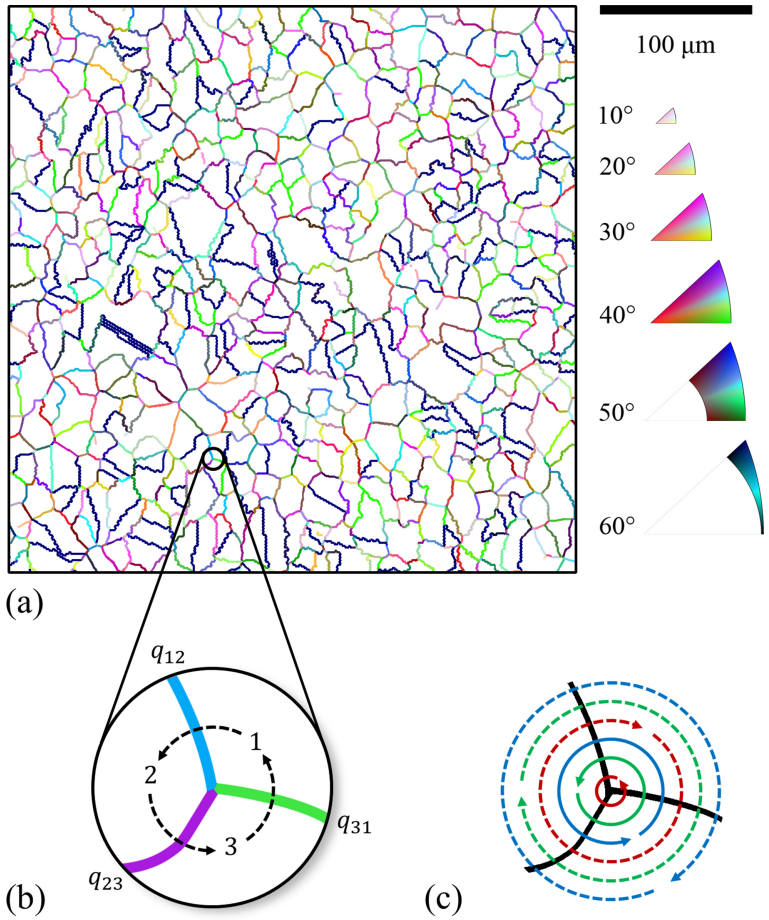

Fig. 1: (a) The grain boundary network of a sample of Inconel 690, representing a global configuration of triple junctions. Grain boundaries in (a) are color coded by their disorientation axis (in the standard stereographic triangle) and angle (see the legend at right) (Patala et al., 2012). (b) The local state of a representative triple junction as indicated by its triple junction misorientations, q_{AB}. The grains coordinating the triple junction are labeled 1, 2, and 3, with dotted arrows defining a circuit that encloses it. Composition of the grain boundary misorientations around such a circuit must result in the identity operation (Eq. 3). (c) All six distinct paths surrounding a triple junction. These correspond to all possible ways of choosing the two independent misorientations coordinating a triple junction, and thus, represent physically equivalent descriptions. Colors distinguish circuits starting in different grains, and line type (solid/dashed) distinguish circuits of different sense.

work. Generalization of our methods and results to include the contribution of grain boundary planes is possible in principle, but constitutes a significant cost in complexity, and will be left for future work.

The misorientation associated with a grain boundary between grains A and B is defined by:

$$q_{AB} = q_A^{-1} q_B \tag{1}$$

where q_A and q_B are the lattice orientations of grains A and B, respectively. In this work we use unit quaternions to represent general three-dimensional rotations. The three independent parameters corresponding to such a rotation may be chosen as the spherical angles of the rotation axis, and the angle of rotation about that axis. These are related to the components of a unit quaternion, $q = [a, b, c, d]$, by (Hamilton, 1844; Mason and Schuh, 2008):

$$\begin{aligned} a &= \cos(\omega/2) \\ b &= \sin(\omega/2)\sin\theta\cos\phi \\ c &= \sin(\omega/2)\sin\theta\sin\phi \\ d &= \sin(\omega/2)\cos\theta \end{aligned} \tag{2}$$

with θ describing the polar angle measured from the positive z-axis, ϕ the azimuthal angle measured from the positive x-axis, and ω the rotation angle.

While there are a total of nine misorientation parameters for a triple junction (three for each misorientation), crystallographic consistency requires that the composition of the misorientations around any closed circuit results in the identity (Bollmann, 1984). For a triple junction coordinated by grains labeled 1, 2, and 3, (see Fig. 1b) this is stated as:

$$q_{12} q_{23} q_{31} = I \tag{3}$$

Therefore, only two of the three misorientations are independent, reducing the total number of misorientation parameters to six. The local state space for triple junction misorientations is, therefore, initially identified with the product space $\mathrm{SO}(3) \times \mathrm{SO}(3)$.

Further consideration of the physical symmetries of a triple junction reveals equivalence relations that both couple and reduce the full misorientation space. Consider a circuit enclosing a triple junction, as depicted in Fig. 1b. One may choose a starting grain and a sense in which to traverse the circuit in any one of $3 \times 2 = 6$ ways, each of which will result in an equivalent description of the triple junction (see Fig. 1c). Consideration of all possible circuits, in conjunction with the constraint of crystallographic consistency, leads to the following set of equivalence relations for the ordered pair of independent misorientations defining a triple junction:

$$F = \left\{ [q_{12}, q_{23}], \left[q_{23}, q_{23}^{-1} q_{12}^{-1}\right], \left[q_{23}^{-1} q_{12}^{-1}, q_{12}\right], \left[q_{12}^{-1}, q_{12} q_{23}\right], \left[q_{12} q_{23}, q_{23}^{-1}\right], \left[q_{23}^{-1}, q_{12}^{-1}\right] \right\} \tag{4}$$

where $[a, b] \equiv \{(q_{12}, q_{23}) \mid (q_{12}, q_{23}) \sim (a, b)\}$. Therefore, for the most general case, the local state space for triple junction misorientations is given by:

$$\mathscr{A}^{(3)} = (\mathrm{SO}(3) \times \mathrm{SO}(3)) / F \tag{5}$$

and is referred to as the triple junction *fundamental zone*, or *asymmetric region*.

If the crystallographic point group, for a material of interest, contains symmetry operations in addition to the identity element, then $\mathscr{A}^{(3)}$ is further reduced. For the purposes of this work, we will demonstrate our methods without including additional crystal symmetry (*i.e.* for triclinic crystals). Generalization to other crystal symmetries is possible, but requires some care in handling the somewhat subtle relationship between crystallographic symmetry and triple junction symmetry.

One noteworthy observation about Eq. 4, is the absence of what is referred to as "grain exchange symmetry" (Patala et al., 2012; Patala and Schuh, 2011). When considering grain boundaries in isolation, the choice of grain A or grain B as the reference orientation is arbitrary, thus one has that $q_{AB} \sim q_{BA}$. However, this is not true when collectively considering grain boundaries that intersect at a triple junction. This becomes readily apparent by replacing q_{12} with q_{21} in Eq. 3 and observing that the result is no longer the identity. Inclusion of "grain exchange symmetry" is tantamount to allowing circuit discontinuities, which violates the constraint of crystallographic consistency. One may indeed reverse the sense of the circuit defining the misorientations around a triple junction, or choose a different starting grain, but once a sense is chosen it must perpetuate until the circuit has closed. As a concrete example, if one exchanges q_{21} for q_{12} one must also exchange q_{32} for q_{23} and q_{13} for q_{31}. In this case Eq. 3 becomes, $q_{21}q_{13}q_{32} = I$ and one may verify that the identity is correctly obtained.

3. Grain Boundary Network Configuration Space

Having considered the design space for the local length scale, we now turn to the design space for the grain boundary network as a whole. A grain boundary network configuration may be characterized by a statistical description of its triple junction states, *i.e.* a distribution function over $\mathscr{A}^{(3)}$. The probability density associated with observing a triple junction characterized by the ordered pair of misorientations $(q_{12}, q_{23}) \in \mathscr{A}^{(3)}$ is given by the six-parameter *triple junction distribution function*[1] (TJDF), $T(q_{12}, q_{23}) = T(\omega_{12}, \theta_{12}, \phi_{12}, \omega_{23}, \theta_{23}, \phi_{23})$.

Abstractly, the complete grain boundary network configuration space is simply the set of all possible functions, $T(q_{12}, q_{23})$, that satisfy the properties of a probability density function and the symmetries described by Eq. 4. We refer to this space as the *triple junction hull*[2] and denote it $\mathscr{M}_H^{(3)}$. A key insight from the work of Adams et al. is that spectral decomposition of the relevant distribution function, in this case $T(q_{12}, q_{23})$, provides parameters with which one may concretely define the boundaries of the space of all such functions (Adams et al., 2012). In other words, the difficulty of defining $\mathscr{M}_H^{(3)}$ directly in function space is greatly alleviated in "frequency" space. In

[1] The full eleven-parameter TJDF would include the boundary plane parameters. For the sake of brevity, and because the context is clear, we will refer to the six-parameter TJDF, which contains only the misorientation information, simply as the TJDF. However, it should be noted that alternative representations of the statistics of triple junction character exist, which include additional crystallographic parameters such as those of the boundary plane normals (Hardy and Field, 2011, 2012).

[2] The notation here is chosen to maintain consistency with and generalize the existing notation in the microstructure design literature. For example, the *texture set* and *texture hull* originally defined in (Adams et al., 2001), are denoted using our scheme as $\mathscr{M}_S^{(1)}$ and $\mathscr{M}_H^{(1)}$ respectively.

order to make use of this insight, it is convenient to discretize $\mathscr{A}^{(3)}$. This immediately suggests a universal form for $T(q_{12}, q_{23})$, given by:

$$T(q_{12}, q_{23}) \approx \sum_{k=1}^{K} p_k \delta^{(3)}\left(q_{12}, {}^k q_{12}\right) \delta^{(3)}\left(q_{23}, {}^k q_{23}\right) \tag{6}$$

where p_k is the probability associated with the k-th ordered pair of misorientations in the discretization, denoted $\left({}^k q_{12}, {}^k q_{23}\right)$, and the approximation becomes exact as $K \to \infty$. The basis functions in Eq. 6 should be regarded as a composite symbol, which denotes a Dirac delta like function respecting the symmetries embodied in Eq. 4. This can be expressed explicitly as:

$$\begin{aligned}
\delta^{(3)}\left(q_{12}, {}^k q_{12}\right) \delta^{(3)}\left(q_{23}, {}^k q_{23}\right) = \frac{1}{6} \Bigg[& \delta\left(q_{12}, {}^k q_{12}\right) \delta\left(q_{23}, {}^k q_{23}\right) \\
& + \delta\left(q_{12}, {}^k q_{23}\right) \delta\left(q_{23}, \left({}^k q_{12} {}^k q_{23}\right)^{-1}\right) \\
& + \delta\left(q_{12}, \left({}^k q_{12} {}^k q_{23}\right)^{-1}\right) \delta\left(q_{23}, {}^k q_{12}\right) \\
& + \delta\left(q_{12}, {}^k q_{12}^{-1}\right) \delta\left(q_{23}, {}^k q_{12} {}^k q_{23}\right) \\
& + \delta\left(q_{12}, {}^k q_{12} {}^k q_{23}\right) \delta\left(q_{23}, {}^k q_{23}^{-1}\right) \\
& + \delta\left(q_{12}, {}^k q_{23}^{-1}\right) \delta\left(q_{23}, {}^k q_{12}^{-1}\right) \Bigg]
\end{aligned} \tag{7}$$

The p_k define a vector space, $M^{(3)}$, over $\mathbb{R}^K$, in which each point, $\boldsymbol{p} = (p_1, p_2, \ldots, p_K)$, represents a grain boundary network (*i.e.* a specific TJDF). Given that the p_k represent probabilities, $M_H^{(3)} \subset M^{(3)}$ is defined by:

$$M_H^{(3)} = \left\{ \boldsymbol{p} \;\middle|\; \boldsymbol{p} = (p_1, p_2, \ldots, p_K),\ 0 \leq p_k,\ \sum_{k=1}^{K} p_k = 1 \right\} \tag{8}$$

which is a standard $(K-1)$-simplex, as shown in Fig. 2a. The change to the roman typeface of $M_H^{(3)}$ is intended to indicate the Dirac basis representation of the triple junction hull, whereas the script typeface of $\mathscr{M}_H^{(3)}$ refers only to the abstract concept, without reference to a specific basis (a distinction that will become important in what follows).

The vertices of $M_H^{(3)}$ correspond to points, ${}^k\boldsymbol{p}$, with only one non-zero component, ${}^k p_k = 1$. These points represent the coefficients of $\delta^{(3)}$ type microstructures centered on $\left({}^k q_{12}, {}^k q_{23}\right)$. We refer to this set of points as the *triple junction set*, $M_S^{(3)} \subset M_H^{(3)} \subset M^{(3)}$, which may be defined mathematically by:

$$M_S^{(3)} = \left\{ {}^k\boldsymbol{p} \;\middle|\; {}^k\boldsymbol{p} = \left({}^k p_1, {}^k p_2, \ldots, {}^k p_K\right),\ {}^k p_r = \delta_{rk},\ k \in [1, K] \right\} \tag{9}$$

It is clear that $M_H^{(3)}$ is simply the convex hull of $M_S^{(3)}$, which is the reason for this nomenclature. Because of the simplicity of the geometry of this definition of $M_H^{(3)}$ it is efficient to sample from and easy to explore. However, another definition also proves to be important.

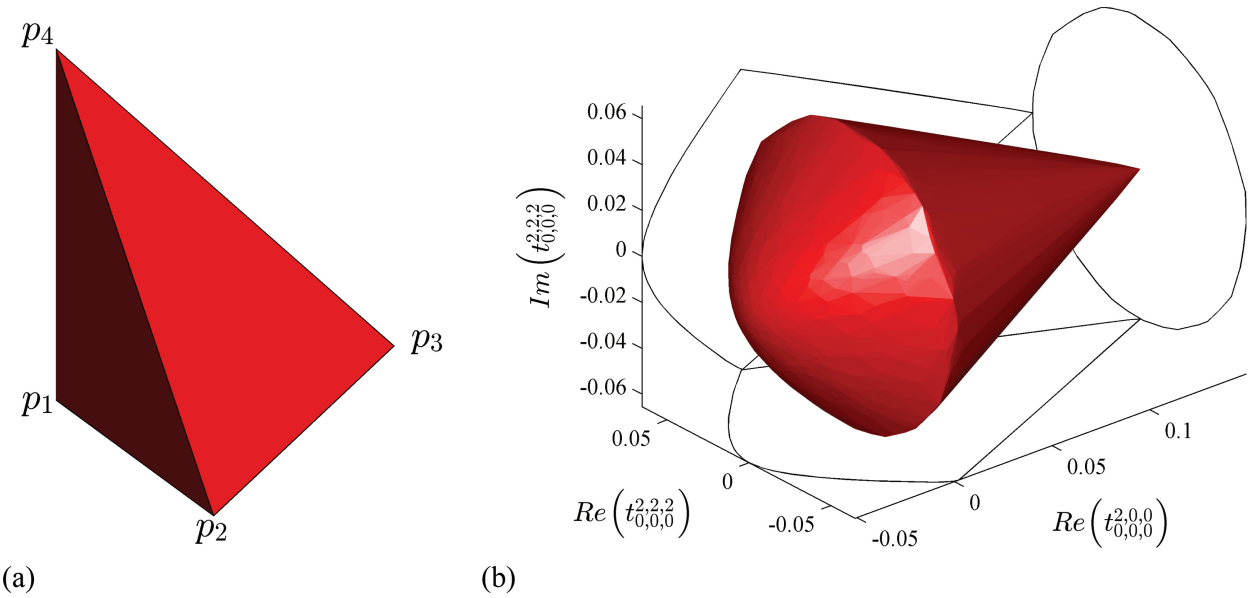

(a) (b)

Fig. 2: (a) The triple junction hull, $M_H^{(3)}$, in the discrete basis with $K = 4$, corresponding to the standard 3-simplex, or tetrahedron. The vertices are points for which the corresponding $p_k = 1$ and all others are 0, edges are points for which two of the p_k are non-zero, faces correspond to points for which three of the p_k are non-zero, and the interior is populated by points for which all of the p_k are non-zero. (b) Orthogonal projection of $m_H^{(3)}$ in the first three non-trivial dimensions. Two-dimensional projections are also shown as outlines for clarity.

Alternatively to Eq. 6, the TJDF may also be expressed as a generalized Fourier series in the basis of bi-polar hyperspherical harmonics (Johnson and Schuh, 2013):

$$T(q_{12}, q_{23}) = \sum_{\substack{n_1,\lambda_{12},\mu_{12} \\ n_3,\lambda_{23},\mu_{23}}} t^{n_3,\lambda_{23},\mu_{23}}_{n_1,\lambda_{12},\mu_{12}} Z^{n_1}_{\lambda_{12},\mu_{12}}(q_{12})\, Z^{n_3}_{\lambda_{23},\mu_{23}}(q_{23}) \tag{10}$$

where the coefficients, $t^{n_3,\lambda_{23},\mu_{23}}_{n_1,\lambda_{12},\mu_{12}}$, may be computed by the inner product:

$$t^{n_3,\lambda_{23},\mu_{23}}_{n_1,\lambda_{12},\mu_{12}} = \oint T(q_{12}, q_{23})\, Z^{n_1}{}^*_{\lambda_{12},\mu_{12}}(q_{12})\, Z^{n_3}{}^*_{\lambda_{23},\mu_{23}}(q_{23}) \tag{11}$$

In Eq. 11, * denotes complex conjugation, and $\oint$ denotes integration over the entire domain, $S^3 \times S^3$, with respect to the appropriate invariant measure (Johnson and Schuh, 2013), which is omitted for brevity. Eq. 11 represents a generalized Fourier transform, with Eq. 10 providing its inverse. We emphasize that Eq. 10 is completely general, and triple junction statistics of *any* microstructure may be expressed in this form, regardless of the presence or absence of spatial correlations. In this basis, the $t^{n_3,\lambda_{23},\mu_{23}}_{n_1,\lambda_{12},\mu_{12}}$ define an infinite-dimensional vector space, $m^{(3)}$, over $\mathbb{C}^\infty$, in which each point, $\boldsymbol{t} = \left(t^{0,0,0}_{0,0,0}, t^{0,0,0}_{2,0,0}, \ldots\right)$, represents a grain boundary network.

Using Eq. 11 we can take the Fourier transform of Eq. 6, which results in:

$$t^{n_3,\lambda_{23},\mu_{23}}_{n_1,\lambda_{12},\mu_{12}} \approx \sum_{k=1}^{K} {p_k}^k t^{n_3,\lambda_{23},\mu_{23}}_{n_1,\lambda_{12},\mu_{12}} \tag{12}$$

where ${}^k t^{n_3,\lambda_{23},\mu_{23}}_{n_1,\lambda_{12},\mu_{12}}$ are the Fourier coefficients of $\delta^{(3)}\left(q_{12}, {}^k q_{12}\right)\delta^{(3)}\left(q_{23}, {}^k q_{23}\right)$.

In light of Eq. 12, alternate definitions of $M_S^{(3)}$ and $M_H^{(3)}$ may be given, respectively, by:

$$
\begin{aligned}
m_S^{(3)} = \Bigg\{ {}^k\boldsymbol{t} \;\Big|\; {}^k\boldsymbol{t} = \left({}^k t^{0,0,0}_{0,0,0}, {}^k t^{0,0,0}_{2,0,0}, {}^k t^{0,0,0}_{2,1,-1}, \ldots, {}^k t^{6,3,-2}_{4,2,1}, \ldots\right), \\
{}^k t^{n_3,\lambda_{23},\mu_{23}}_{n_1,\lambda_{12},\mu_{12}} = \oint \delta^{(3)}\left(q_{12}, {}^k q_{12}\right)\delta^{(3)}\left(q_{23}, {}^k q_{23}\right) {Z^{n_1}_{\lambda_{12},\mu_{12}}}^{*}(q_{12})\, {Z^{n_3}_{\lambda_{23},\mu_{23}}}^{*}(q_{23}), \\
\left({}^k q_{12}, {}^k q_{23}\right) \in \mathscr{A}^{(3)},\ k \in [1, K] \Bigg\}
\end{aligned}
\tag{13}
$$

$$
m_H^{(3)} = \left\{ \boldsymbol{t} \;\middle|\; \boldsymbol{t} \approx \sum_{k=1}^{K} p_k\, {}^k\boldsymbol{t},\ {}^k\boldsymbol{t} \in m_S^{(3)},\ 0 \le p_k,\ \sum_{k=1}^{K} p_k = 1 \right\} \tag{14}
$$

where the lower-case $m_S^{(3)}$ and $m_H^{(3)}$ are chosen to distinguish the Fourier representation of the triple junction set and triple junction hull, respectively, from their representation in the Dirac basis, $M_S^{(3)}$ and $M_H^{(3)}$. Geometrically, $m_H^{(3)}$ represents a closed convex polytope inhabiting infinite dimensional Fourier space, whose vertices are the set $m_S^{(3)}$, and clearly, $m_S^{(3)} \subset m_H^{(3)} \subset m^{(3)}$. Considering the real and imaginary components of the $t^{n_3,\lambda_{23},\mu_{23}}_{n_1,\lambda_{12},\mu_{12}}$ as separate dimensions, Fig. 2b displays an orthogonal projection of $m_H^{(3)}$ in the first three non-trivial Fourier dimensions.

In the preceding derivation we temporarily ignored a somewhat subtle, albeit important, issue regarding the convexity of the triple junction hull. Eqns. 8 and 14 define the triple junction hull as the convex hull of the triple junction set. It is evident that the coefficients of any TJDF, whether in the Dirac or Fourier bases, may be expressed as a convex linear combination of those of the triple junction set. However, it is not immediately obvious that the converse is true, *i.e* that every convex combination, so formed, generates a TJDF that is physically realizable. This point is essential to establish because if there exist certain, otherwise valid, $\boldsymbol{p}$ that do not correspond to physically realizable microstructures, then the triple junction hull is not truly convex, and it contains non-physical regions, corresponding to non-feasible design solutions. If such were the case it would significantly hamper the use of the foregoing methodology, if not altogether thwart it.

In order to prove the convexity of the triple junction hull, we first give an example of a grain boundary network composed of triple junctions that all possess the same local state. Fig. 3 shows a hypothetical microstructure consisting of columnar grains, each possessing one of three possible orientations. In such a microstructure every triple junction is coordinated by each of the three possible orientations, and hence all triple junctions are identical.

In order to prove the convexity of the triple junction hull, it is enough to show that there exists at least one physically realizable microstructural instantiation for any $\boldsymbol{p} \in M_H^{(3)}$. One procedure to construct a microstructure corresponding to an arbitrary $\boldsymbol{p}$ is by "gluing" together a succession of lamellae of the single triple junction state microstructures, depicted in Fig. 3, whose relative sizes are given by the corresponding p_k. Fig. 4 shows an example of such a microstructure in which each lamella is given a different color scheme. The target values of the p_k are, respectively, $\boldsymbol{p} = (0.1875, 0.0625, 0.4375, 0.3125)$. At the interface between lamellae there are triple junctions that do not correspond to any of the target states, as shown in the interfacial detail views in Fig. 4,

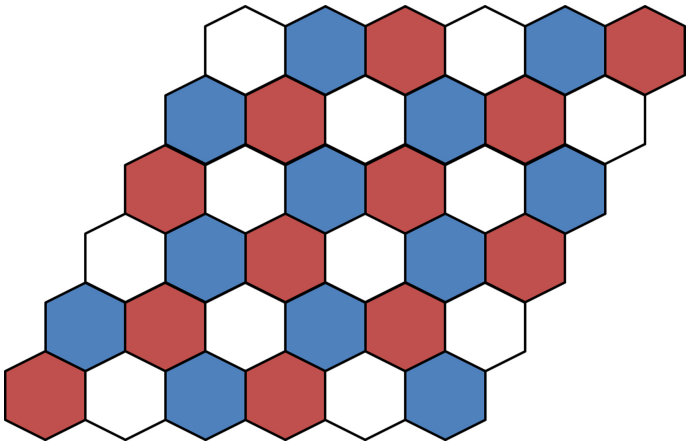

Fig. 3: A schematic of a columnar microstructure in which every triple junction possesses the same state. The three grain orientations are distinguished by color (red, blue, and white).

which are artifacts of the "gluing" operation. Consequently, the p_k do not achieve their target values, as demonstrated by the actual values shown in Fig. 4. However, as the system size grows, the fraction of triple junctions inhabiting the interfacial regions decreases as ${N_{tj}}^{-1/2}$, where N_{tj} is the total number of triple junctions in the system. Thus, in the limit as $N_{tj} \to \infty$ the target distribution is realized exactly, and this is true for any arbitrary $\boldsymbol{p}$. Therefore, we conclude that the triple junction hull is formally convex. The coefficients of any TJDF may be decomposed into a convex combination of the coefficients of the triple junction set, and every convex combination is physically realizable. The convexity of $\mathscr{M}_H^{(3)}$ implies that any path through the design space will be entirely composed of physically realizable microstructural states; thus, during the design and optimization process there is no danger of encountering any unphysical solutions. Furthermore, this convexity permits efficient exploration of the design space *via* the p_k, for which calculation and tests of feasibility are computationally inexpensive.

It is worth noting that, for triple junctions, this construction is completely general. For an arbitrarily chosen state, characterized by the ordered pair of misorientations (q_{12}, q_{23}), one may generate a microstructure in which all triple junctions are in the chosen state. However, it is not possible to generate a microstructure in which all grain boundaries possess the same, arbitrarily chosen, state (q_{12}). This fact suggests that a grain boundary hull, $\mathscr{M}_H^{(2)}$, would be non-convex, which highlights the convenience of designing grain boundary networks in the context of triple junctions instead of directly focusing on grain boundaries.

4. Texture & Topology

The tools that we have developed here are intended to aid in the design of grain boundary networks. The triple junction hull defines the design space, and provides the necessary parameters (the p_k or $t^{n_3,\lambda_{23},\mu_{23}}_{n_1,\lambda_{12},\mu_{12}}$) to explore its entirety in search of grain boundary networks with enhanced physical properties.

While all points in the triple junction hull are feasible, it is not necessarily true that they will all be equally straightforward to synthesize experimentally. Ultimately, fabrication of a particular

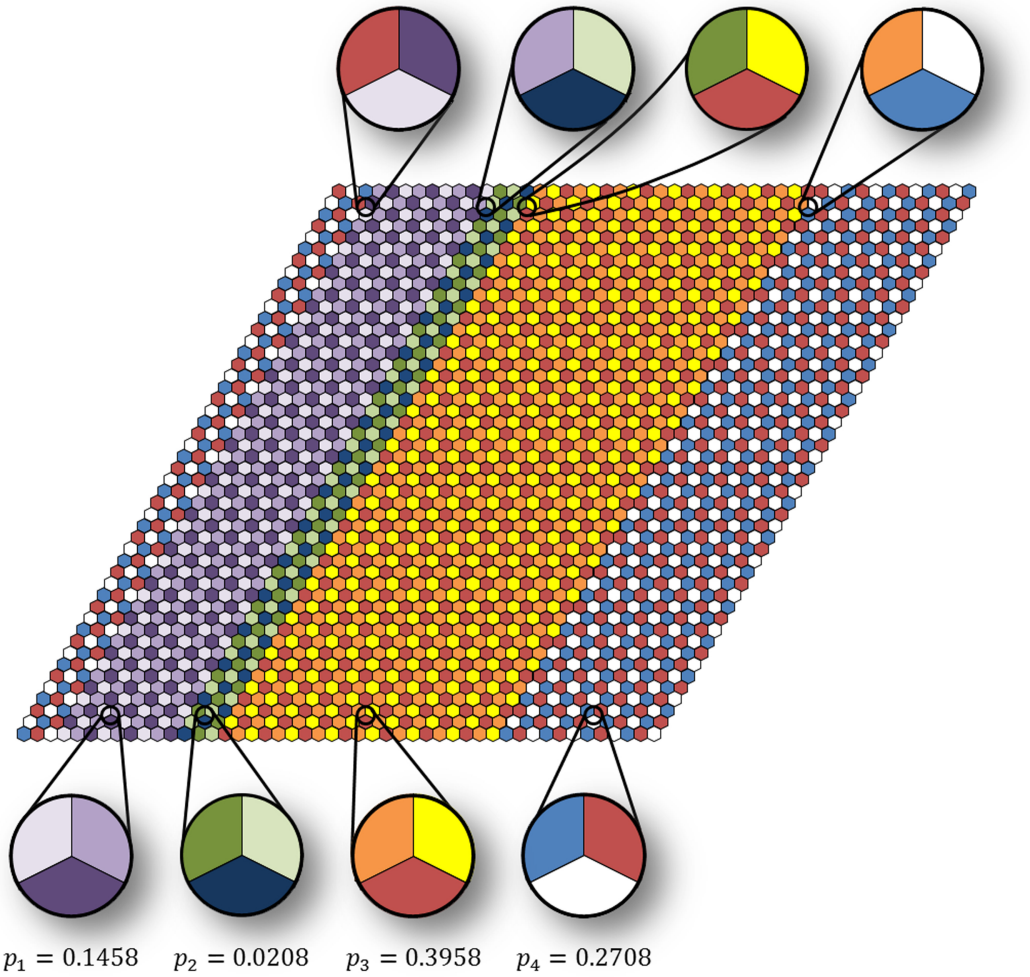

Fig. 4: A microstructure with columnar grains and periodic boundary conditions, formed by "gluing" together four lamellae, each with a single triple junction state. The triple junction state of each lamella is shown in the lower detail views, along with the actual values of p_k that are attained. For ease of visualization the orientations of the incident grains are colored rather than the grain boundaries themselves. The states of triple junctions inhabiting the interfaces are shown in the upper detail views.

grain boundary network amounts to controlling the orientation of each grain and its relative position in the microstructure. Because most standard processing routes provide control primarily over the distribution of grain orientations, it is useful to consider how far one might get through the control of crystallographic texture alone.

In the absence of spatial correlations of grain orientation, it is possible to derive an *uncorrelated* TJDF, which we denote $\widetilde{T}(q_{12}, q_{23})$, and whose coefficients may be obtained directly from those of the orientation distribution function (ODF) according to[3] (Johnson and Schuh, 2013):

$$\widetilde{t}^{n_3,\lambda_{23},\mu_{23}}_{n_1,\lambda_{12},\mu_{12}} = \sum_{\substack{l_1,m_1 \\ n_2,l_2,m_2 \\ l_3,m_3 \\ \lambda_1,\mu_1 \\ \lambda_3,\mu_3}} (-1)^{\lambda_{12}-\lambda_3+\mu_3} c^{n_1}_{l_1,m_1} c^{n_2}_{l_2,m_2} c^{n_3}_{l_3,m_3} A^{n_1,l_1,m_1}_{\lambda_1,\mu_1,\lambda_{12},\mu_{12}} A^{n_3,l_3,m_3}_{\lambda_3,\mu_3,\lambda_{23},\mu_{23}} L^{n_3,\lambda_3,-\mu_3}_{n_1,\lambda_1,\mu_1;n_2,l_2,m_2} \tag{15}$$

where the $c^n_{l,m}$ are the coefficients of an ODF expressed as a generalized Fourier series in the basis of hyperspherical harmonics, the $A^{n,l,m}_{l_2,m_2,l_1,m_1}$ are the coefficients of the hyperspherical harmonic addition theorem (Mason, 2009) as defined in Appendix B.1, and the $L^{n_3,l_3,m_3}_{n_1,l_1,m_1;n_2,l_2,m_2}$ are the coefficients of the hyperspherical harmonic linearization theorem defined in Appendix B.2.

Consider all possible simultaneous values that the $\widetilde{t}^{n_3,\lambda_{23},\mu_{23}}_{n_1,\lambda_{12},\mu_{12}}$ may take. This represents a subset of $m^{(3)}_H$, which we denote $\widetilde{m}^{(3)}_H$, and whose size, relative to $m^{(3)}_H$ provides an estimate for how much of the grain boundary network design space is accessible through the control of texture alone. In order to measure $\widetilde{m}^{(3)}_H$, we must first introduce the concepts of the *texture set* and *texture hull*[4] (Adams et al., 2001, 2012; Fast et al., 2008) and provide their mathematical definitions in the context of the hyperspherical harmonic expansion.

As described by Mason (2009), an ODF may be expressed as a linear combination of hyperspherical harmonics:

$$f(q) = \sum_{n=0,2,\ldots}^{\infty} \sum_{l=0}^{n} \sum_{m=-l}^{l} c^n_{l,m} Z^n_{l,m}(q) \tag{16}$$

where the coefficients, $c^n_{l,m}$, correspond to those appearing in Eq. 15. The texture set, which we denote as $m^{(1)}_S$, consists of the Fourier representation of all possible single crystal textures. For the case of materials with triclinic crystal and sample symmetry, $m^{(1)}_S$ can be expressed as:

$$m^{(1)}_S = \left\{ {}^j\boldsymbol{c} \;\middle|\; {}^j\boldsymbol{c} = \left({}^jc^0_{0,0}, {}^jc^2_{0,0}, {}^jc^2_{1,-1}, \ldots \right),\ {}^jc^n_{l,m} = {Z^n_{l,m}}^*\left({}^jq \right),\ {}^jq \in SO(3),\ j \in [1, J] \right\} \tag{17}$$

The texture hull, $m^{(1)}_H$, which delineates the space of all possible crystallographic textures, is simply the convex hull of $m^{(1)}_S$:

$$m^{(1)}_H = \left\{ \boldsymbol{c} \;\middle|\; \boldsymbol{c} \approx \sum_{j=1}^{J} p'_j {}^j\boldsymbol{c},\ {}^j\boldsymbol{c} \in m^{(1)}_S,\ 0 \leq p'_j,\ \sum_{j=1}^{J} p'_j = 1 \right\} \tag{18}$$

[3]The form of Eq. 15 is somewhat different than what is found in Eq. 15 of Johnson and Schuh (2013), though the two are equivalent. The form given in Johnson and Schuh (2013) is more efficient computationally, while Eq. 15 of the present work is more compact from a notational perspective.

[4]These concepts were first introduced by Adams et al. (2001) as a specific case of the more general concepts of *microstructure set* and *microstructure hull*.

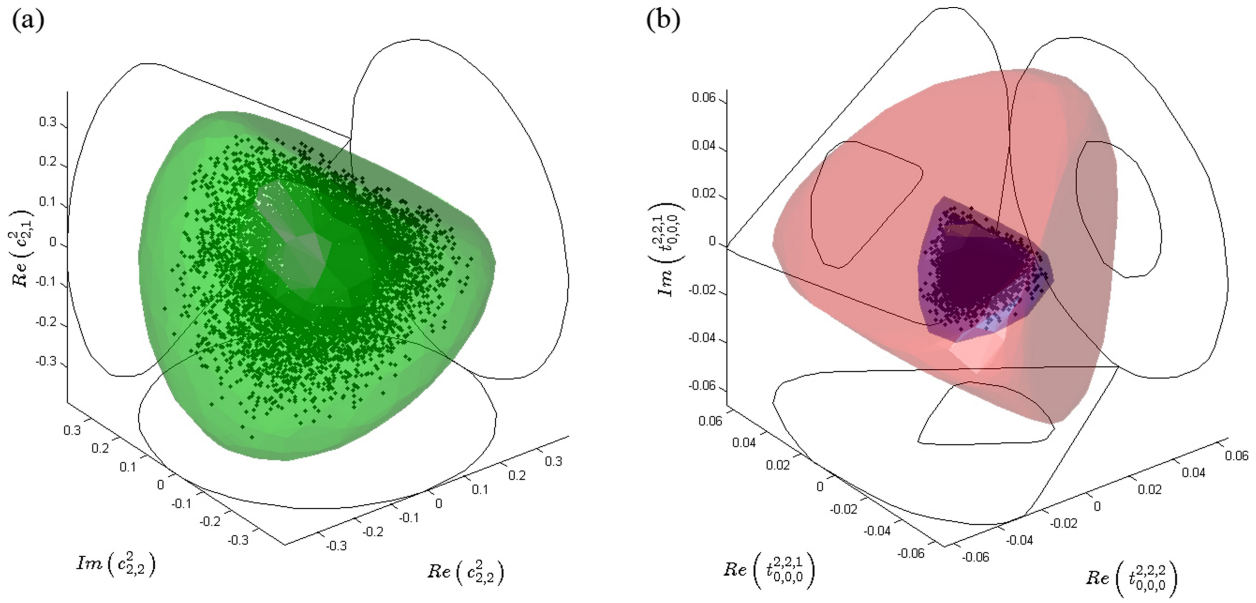

Fig. 5: In (a) The green surface contains a three-dimensional orthogonal projection of $m_H^{(1)}$, and the points are samples, $\boldsymbol{c}_s$, taken uniformly from the six-dimensional orthogonal projection of $m_H^{(1)}$, as defined in Section 4. In (b) the red surface contains a three-dimensional orthogonal projection of $m_H^{(3)}$, the blue surface corresponds to $\widetilde{m}_H^{(3)}$, and the points are the $\boldsymbol{t}_s$ obtained from the $\boldsymbol{c}_s$ *via* Eq. 15.

Having defined $m_H^{(1)}$, we use the following procedure to quantify the size of $\widetilde{m}_H^{(3)}$ relative to $m_H^{(3)}$. First, we generate S samples, $\boldsymbol{c}_s$, $s \in [1, S]$, uniformly distributed within $m_H^{(1)}$. We then use Eq. 15 to compute $\widetilde{\boldsymbol{t}}_s$ for each of the ODFs so generated. The convex hull of all of the $\widetilde{\boldsymbol{t}}_s$ is then an approximation of $\widetilde{m}_H^{(3)}$.

Due to the computational cost of defining high-dimensional convex hulls and generating uniform samples over them, we consider only terms up to $\max(n_1, n_3) = 2$. In this case there are six independent non-degenerate dimensions for $m_H^{(3)}$, as can be verified through the use of Eqs. A.4 and A.11. They are: $\mathrm{Re}\left(t^{2,0,0}_{0,0,0}\right)$, $\mathrm{Re}\left(t^{2,2,0}_{0,0,0}\right)$, $\mathrm{Re}\left(t^{2,2,1}_{0,0,0}\right)$, $\mathrm{Im}\left(t^{2,2,1}_{0,0,0}\right)$, $\mathrm{Re}\left(t^{2,2,2}_{0,0,0}\right)$, $\mathrm{Im}\left(t^{2,2,2}_{0,0,0}\right)$. According to Eq. 15, they collectively depend only on the following five ODF coefficients: $c^0_{0,0}$, $c^2_{0,0}$, $c^2_{2,0}$, $c^2_{2,1}$, $c^2_{2,2}$. Because $c^0_{0,0} = \left(2\pi^2\right)^{-1/2}$ is a constant, and $c^n_{l,0}$ is strictly real for even l, by virtue of the reality condition for ODFs (Eq. A.3), we are only concerned with the orthogonal projection of $m_H^{(1)}$ defined by the following six dimensions: $\mathrm{Re}\left(c^2_{0,0}\right)$, $\mathrm{Re}\left(c^2_{2,0}\right)$, $\mathrm{Re}\left(c^2_{2,1}\right)$, $\mathrm{Im}\left(c^2_{2,1}\right)$, $\mathrm{Re}\left(c^2_{2,2}\right)$, $\mathrm{Im}\left(c^2_{2,2}\right)$.

We numerically converted the vertex representation of $m_H^{(1)}$, given in Eq. 18, to its equivalent *half-space* (or facet) representation by means of Jacobson's *vert2lcon.m* code (Jacobson, 2012). Subsequently, we used the *hit-and-run* algorithm (see Kroese et al., 2011, pp. 40-44), as implemented in Benham's *cprnd.m* (Benham, 2012), to sample $S = 10^6$ points uniformly within the convex polytope defined by the above-mentioned six-dimensional orthogonal projection of $m_H^{(1)}$. We performed all computations using MATLAB (2012). A three-dimensional orthogonal projection of $m_H^{(1)}$ and the samples that were generated are shown in Fig. 5a. We then computed the $\widetilde{\boldsymbol{t}}_s$ from Eq. 15, which are shown, together with their convex hull, in Fig. 5b. Let $\widetilde{\mu}_d/\mu_d \equiv \mu_d\left(\widetilde{m}_H^{(3)}\right)/\mu_d\left(m_H^{(3)}\right)$

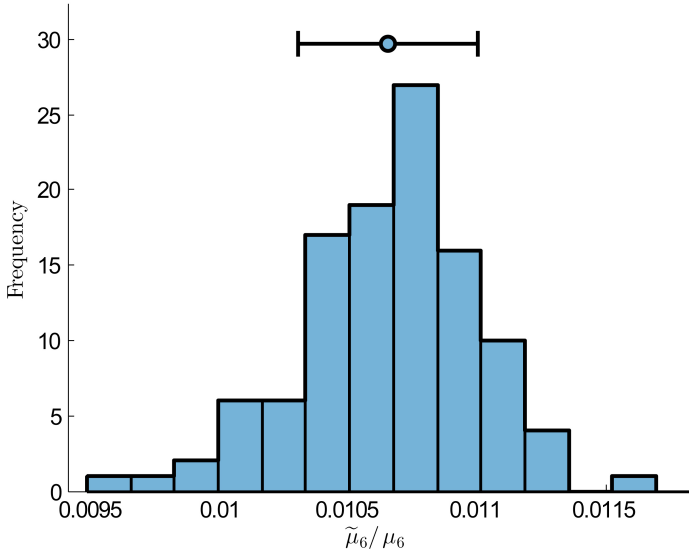

Fig. 6: Histogram of the ratio of the six-dimensional measures of $\widetilde{m}_H^{(3)}$ and $m_H^{(3)}$. The mean and standard deviation are also plotted.

denote the ratio of the d-dimensional measures of $\widetilde{m}_H^{(3)}$ and $m_H^{(3)}$. With 110 repetitions of this process, we found $\widetilde{\mu}_6/\mu_6 = 0.0107$ with a standard deviation of 0.0004 (see Fig. 6). This is to say that, restricting our attention to the six lowest order dimensions, only about 1% of all possible TJDFs are accessible in the absence of spatial correlations in grain orientation. One should note, however, that the small relative size of $\widetilde{m}_H^{(3)}$ is largely a result of dimensionality. As is apparent from Fig. 5b, for a given dimension, $\widetilde{m}_H^{(3)}$ covers roughly half the range of $m_H^{(3)}$; more specifically, $\widetilde{\mu}_1/\mu_1 = 0.4193 \pm 0.0444$, averaged over all six dimensions and all trials. The quantity $\widetilde{\mu}_1/\mu_1$ may be regarded as the average probability that a given coefficient from a randomly selected TJDF will lie within the bounds of $\widetilde{m}_H^{(3)}$. Even if we had $\widetilde{\mu}_1/\mu_1 = 1-\epsilon$ for arbitrarily small $\epsilon > 0$, so long as the number of dimensions for which $\widetilde{\mu}_1/\mu_1 < 1$ is not finite, then $\lim_{d\to\infty} \widetilde{\mu}_d/\mu_d = 0$. So, indeed, $\widetilde{m}_H^{(3)}$ *is* smaller than $m_H^{(3)}$, however, *how much* smaller depends upon how many dimensions one considers, and, since in all practical cases one will truncate the series defining $T(q_{12}, q_{23})$ to exclude the less important higher-order terms, this limitation is at least partially ameliorated.

Another salient point that can be observed in Fig. 5b is that $\widetilde{m}_H^{(3)}$ is concentrated about the origin. In this space, the origin corresponds to the uniform TJDF, in which all types of triple junction are equally likely, and for which the only non-zero coefficient is $t_{0,0,0}^{0,0,0} = \left(2\pi^2\right)^{-1}$. This means that the TJDFs that *are* accessible in the absence of spatial correlations correspond to somewhat less exotic TJDFs than those that are possible with spatial correlations.

5. Conclusions

The character and connectivity of grain boundaries in polycrystalline materials controls a host of materials properties and phenomena. Empirical evidence from grain boundary engineering (GBE) studies suggests the possibility of enhancing materials properties through manipulation of

the grain boundary network in strategic ways. At present, however, general understanding of grain boundary network structure and its effect on materials properties is limited. This has precluded the inductive design of grain boundary networks.

In this work we have highlighted the intrinsically multi-scale nature of grain boundary network design. We identified triple junctions as convenient topological features corresponding to a local length scale. We defined the local state space for triple junctions and provided the equivalence relations that define its fundamental zone, $\mathscr{A}^{(3)}$. We also defined the global configuration space for grain boundary networks, $\mathscr{M}_H^{(3)}$, and demonstrated its convexity. These tools allow one to explore the complete universe of grain boundary networks in search of application specific globally optimal network configurations. The importance of these tools is further highlighted by the fact that existing GBE processing methods are only effective for materials that twin readily. The prospect of inductive grain boundary network design suggests the opportunity to achieve unprecedented properties enhancements in materials that are not amenable to traditional GBE.

Additionally, we investigated the relative size of the portion of the grain boundary network design space that is accessible in the absence of spatial correlations, $\widetilde{m}_H^{(3)}$. We found $\widetilde{m}_H^{(3)}$ to be a small fraction of the size of $m_H^{(3)}$. The implications of these results are significant: the control and manipulation of crystallographic texture alone is insufficient to access the vast majority of the grain boundary network design space. Furthermore, spatial correlations of grain orientation expand this space and are required to reach the more extreme grain boundary network configurations. At the same time, the fact that higher-order terms in the Fourier series of a TJDF are decreasingly important, indicates that $\widetilde{m}_H^{(3)}$ is of more significance than first impressions might suggest.

6. Acknowledgments

This work was supported by the US Department of Energy (DOE), Office of Basic Energy Sciences under award no. DE-SC0008926. O.K.J. acknowledges support from the Department of Defense (DoD) through the National Defense Science & Engineering Graduate Fellowship (NDSEG) Program.

Appendix A. Relations for the Coefficients of ODFs and TJDFs

Constraints imposed upon a function that is to be expressed in the form of a generalized Fourier series result in constraints upon the values of and relationships between the coefficients. In this section we give several of the most useful of these relations for ODFs and TJDFs. The existence of such relations allows one to identify which coefficients are independent, and therefore reduces the computational cost of their evaluation. Furthermore, these relations reduce the dimensionality of $m_H^{(3)}$, thus greatly reducing the computational cost of exploring the design space.

Appendix A.1. The Reality Condition

Because an ODF is a probability density function it must be strictly real valued, *i.e.* $f^*(q) = f(q)$. Employing the expansion of Eq. 16 for both sides of this expression results in:

$$\sum_{n,l,m} {c_{l,m}^n}^* {Z_{l,m}^n}^*(q) = \sum_{n,l,m} c_{l,m}^n Z_{l,m}^n(q) \tag{A.1}$$

Making use of the complex conjugation identity for the hyperspherical harmonics (Mason, 2009) one has:

$$\sum_{n,l,m} (-1)^{l+m} {c_{l,m}^n}^* Z_{l,-m}^n(q) = \sum_{n,l,m} c_{l,m}^n Z_{l,m}^n(q) \tag{A.2}$$

By changing indices on the left-hand side ($m \leftrightarrow -m$), setting the coefficients equal term by term, and taking the complex conjugate of both sides, one arrives at:

$${c_{l,m}^n}^* = (-1)^{l-m} c_{l,-m}^n \tag{A.3}$$

as a reality condition for the coefficients of an ODF.

The same procedure may be used to obtain the reality condition for a TJDF, with the result being:

$${t_{n_1,\lambda_{12},\mu_{12}}^{n_3,\lambda_{23},\mu_{23}}}^* = (-1)^{\lambda_{12}-\mu_{12}+\lambda_{23}-\mu_{23}} t_{n_1,\lambda_{12},-\mu_{12}}^{n_3,\lambda_{23},-\mu_{23}} \tag{A.4}$$

Appendix A.2. Triple Junction Symmetries

Consider a circuit enclosing a triple junction coordinated by grains labeled 1, 2, and 3 (see Fig. 1b). Without loss of generality, let the circuit begin in grain 1, proceeding next to grain 2, on to grain 3 and finally returning to grain 1. We take, as a convention, the misorientations of the first two grain boundaries that are crossed, q_{12} and q_{23}, to be the two independent misorientations defining the triple junction. Traversing the circuit in the opposite direction results in an equivalent description using the misorientations q_{13} and q_{32}. Thus the TJDF must be invariant with respect to either choice, and we have:

$$\begin{aligned} T(q_{12}, q_{23}) &= T(q_{13}, q_{32}) \\ &= T\left(q_{12}q_{23}, q_{23}^{-1}\right) \end{aligned} \tag{A.5}$$

where the second line is a result of Eq. 3 and the definition of a misorientation. Expanding both sides using Eq. 10 one has:

$$\sum_{\substack{n_1,\lambda_{12},\mu_{12} \\ n_3,\lambda_{23},\mu_{23}}} t_{n_1,\lambda_{12},\mu_{12}}^{n_3,\lambda_{23},\mu_{23}} Z_{\lambda_{12},\mu_{12}}^{n_1}(q_{12})\, Z_{\lambda_{23},\mu_{23}}^{n_3}(q_{23}) = \sum_{\substack{n_1,\lambda_{12},\mu_{12} \\ n_3,\lambda_{23},\mu_{23}}} t_{n_1,\lambda_{12},\mu_{12}}^{n_3,\lambda_{23},\mu_{23}} Z_{\lambda_{12},\mu_{12}}^{n_1}(q_{12}q_{23})\, Z_{\lambda_{23},\mu_{23}}^{n_3}\left(q_{23}^{-1}\right) \tag{A.6}$$

For the sake of typographic economy, and because all subsequent manipulations will be performed exclusively on the right-hand side, we will henceforth omit the left-hand side. The first hyperspherical harmonic on the right-hand side may be expanded using the addition theorem (Eq. B.1), and the second hyperspherical harmonic may be expressed as a function of q_{23} by means of the inversion symmetry relation for hyperspherical harmonics (Eq. C.3 of Johnson and Schuh (2013)), resulting in:

$$\sum_{\substack{n_1,\lambda_{12},\mu_{12} \\ n_3,\lambda_{23},\mu_{23}}} (-1)^{\lambda_{23}} t_{n_1,\lambda_{12},\mu_{12}}^{n_3,\lambda_{23},\mu_{23}} \sum_{\substack{\lambda_1,\mu_1 \\ l_1,m_1}} A_{\lambda_1,\mu_1,l_1,m_1}^{n_1,\lambda_{12},\mu_{12}} Z_{\lambda_1,\mu_1}^{n_1}(q_{12})\, Z_{l_1,m_1}^{n_1}(q_{23})\, Z_{\lambda_{23},\mu_{23}}^{n_3}(q_{23}) \tag{A.7}$$

The product of the two hyperspherical harmonics taking a common argument is then simplified *via* the linearization theorem (Eq. B.3):

$$\sum_{\substack{n_1,\lambda_1,\mu_1\\ n_2,l_2,m_2}} \left[\sum_{\substack{n_3,\lambda_{23},\mu_{23}\\ \lambda_{12},\mu_{12}\\ l_1,m_1}} (-1)^{\lambda_{23}} t^{n_3,\lambda_{23},\mu_{23}}_{n_1,\lambda_{12},\mu_{12}} A^{n_1,\lambda_{12},\mu_{12}}_{\lambda_1,\mu_1,l_1,m_1} L^{n_2,l_2,m_2}_{n_1,l_1,m_1;n_3,\lambda_{23},\mu_{23}} \right] Z^{n_1}_{\lambda_1,\mu_1}(q_{12})\, Z^{n_2}_{l_2,m_2}(q_{23}) \tag{A.8}$$

Finally, relabeling the indices ($\lambda_{12} \leftrightarrow \lambda_1$, $\mu_{12} \leftrightarrow \mu 1$, $n_3 \leftrightarrow n_2$, $\lambda_{23} \leftrightarrow l_2$, $\mu_{23} \leftrightarrow m_2$), and setting the coefficients of Eq. A.8 equal to those of the left-hand side of Eq. A.6, term by term, results in the following:

$$t^{n_3,\lambda_{23},\mu_{23}}_{n_1,\lambda_{12},\mu_{12}} = \sum_{\substack{n_2,l_2,m_2\\ \lambda_1,\mu_1\\ l_1,m_1}} (-1)^{l_2} t^{n_2,l_2,m_2}_{n_1,\lambda_1,\mu_1} A^{n_1,\lambda_1,\mu_1}_{\lambda_{12},\mu_{12},l_1,m_1} L^{n_3,\lambda_{23},\mu_{23}}_{n_1,l_1,m_1;n_2,l_2,m_2} \tag{A.9}$$

as the *circuit sense symmetry* relation for the coefficients of a TJDF.

Following the same procedure for the case in which the sense is not reversed, but the starting grain is changed results in the following:

$$t^{n_3,\lambda_{23},\mu_{23}}_{n_1,\lambda_{12},\mu_{12}} = \sum_{\substack{n_2,l_2,m_2\\ \lambda_1,\mu_1\\ l_1,m_1}} (-1)^{\lambda_1} t^{n_1,\lambda_1,\mu_1}_{n_2,l_2,m_2} A^{n_1,\lambda_1,\mu_1}_{\lambda_{12},\mu_{12},l_1,m_1} L^{n_3,\lambda_{23},\mu_{23}}_{n_1,l_1,m_1;n_2,l_2,m_2} \tag{A.10}$$

as the *circuit start symmetry* relation.

The somewhat complicated nature of the expressions in Eqs. A.9 – A.10, renders them impractical for most uses. However, if one follows the same procedure, but considers the simultaneous operations of a change in starting grain and change of circuit sense, one arrives at the following simple expression:

$$t^{n_1,\lambda_{12},\mu_{12}}_{n_3,\lambda_{23},\mu_{23}} = (-1)^{\lambda_{12}+\lambda_{23}} t^{n_3,\lambda_{23},\mu_{23}}_{n_1,\lambda_{12},\mu_{12}} \tag{A.11}$$

The use of Eq. A.11 obviates the need for Eqs. A.9 – A.10, as it simultaneously enforces both types of symmetry condition. Furthermore, Eq. A.11 is clearly preferable for most applications, such as the identification of the independent TJDF coefficients, which is its primary use in the present work (see Section 4).

Appendix B. Mathematical Theorems

Here we provide several mathematical results that are both necessary for the main results of this paper and of great use generally for the mathematical treatment of microstructures.

Appendix B.1. Addition Theorem

Mason (2009) provided an addition theorem for the hyperspherical harmonics, which we reproduce here in order to make our notation, which differs from that of Mason, explicit. A hyperspherical harmonic, whose argument is the result of the composition of two rotations, may be expanded according to:

$$Z^n_{l,m}(q_2 q_1) = \sum_{\substack{l_2,m_2 \\ l_1,m_1}} A^{n,l,m}_{l_2,m_2,l_1,m_1} Z^n_{l_2,m_2}(q_2)\, Z^n_{l_1,m_1}(q_1) \tag{B.1}$$

with the coefficients of the addition theorem provided by:

$$A^{n,l,m}_{l_2,m_2,l_1,m_1} = (-1)^{-l_2-l_1} \sqrt{\frac{2\pi^2\,(2l_2+1)\,(2l_1+1)}{n+1}} C^{l,m}_{l_2,m_2,l_1,m_1} \begin{Bmatrix} l & l_2 & l_1 \\ n/2 & n/2 & n/2 \end{Bmatrix} \tag{B.2}$$

Appendix B.2. Linearization Theorem

Orthogonal polynomials come equipped with a linearization theorem, which allows one to express the product of two polynomials of like argument, but differing degrees (and possibly different parameters), as a linear combination of other polynomials (Park, 2006). The linearization theorem for the hyperspherical harmonics takes the following form:

$$Z^{n_1}_{l_1,m_1} Z^{n_2}_{l_2,m_2} = \sum_{n_3=|n_1-n_2|}^{n_1+n_2} \sum_{l_3=0}^{n_3} \sum_{m_3=-l_3}^{l_3} L^{n_3,l_3,m_3}_{n_1,l_1,m_1;n_2,l_2,m_2} Z^{n_3}_{l_3,m_3} \tag{B.3}$$

In Eq. B.3 all of the hyperspherical harmonics take identical arguments, which are omitted for brevity. The linearization coefficient, $L^{n_3,l_3,m_3}_{n_1,l_1,m_1;n_2,l_2,m_2}$, is found by multiplying both sides by the complex conjugate of another hyperspherical harmonic of the same argument and integrating over the entire domain:

$$\oint Z^{n_1}_{l_1,m_1} Z^{n_2}_{l_2,m_2} Z^{n_3'*}_{l_3',m_3'} = \sum_{n_3=|n_1-n_2|}^{n_1+n_2} \sum_{l_3=0}^{n_3} \sum_{m_3=-l_3}^{l_3} L^{n_3,l_3,m_3}_{n_1,l_1,m_1;n_2,l_2,m_2} \oint Z^{n_3}_{l_3,m_3} Z^{n_3'*}_{l_3',m_3'} \tag{B.4}$$

The integral on the right-hand side is equal to $\delta_{n_3,n_3'}\delta_{l_3,l_3'}\delta_{m_3,m_3'}$ by the orthonormality of the hyperspherical harmonics, which results in:

$$L^{n_3,l_3,m_3}_{n_1,l_1,m_1;n_2,l_2,m_2} = \oint Z^{n_1}_{l_1,m_1} Z^{n_2}_{l_2,m_2} Z^{n_3*}_{l_3,m_3} \tag{B.5}$$

In previous work (Johnson and Schuh, 2013), we provided the solution to integrals of the form that appears in Eq. B.5. Substituting these results into Eq. B.5 and simplifying yields:

$$L^{n_3,l_3,m_3}_{n_1,l_1,m_1;n_2,l_2,m_2} = \sqrt{\frac{(n_1+1)\,(n_2+1)\,(n_3+1)\,(2l_1+1)\,(2l_2+1)}{2\pi^2}} C^{l_3,m_3}_{l_1,m_1,l_2,m_2} \begin{Bmatrix} n_1/2 & n_2/2 & n_3/2 \\ n_1/2 & n_2/2 & n_3/2 \\ l_1 & l_2 & l_3 \end{Bmatrix} \tag{B.6}$$

Meremianin (2006) derived a similar result for what he referred to as the *spherical-type hyperspherical harmonics* or *C-harmonics*, $C_{n,l,m}$, which are related to the hyperspherical harmonics used in this work by a normalization factor[5]: $Z^n_{l,m} = \sqrt{\frac{n+1}{2\pi^2}} C_{n,l,m}$. Meremianin refers to his result as the *C-type Clebsch-Gordan Coefficients*, $C^{n_3 l_3 m_3}_{n_1 l_1 m_1; n_2 l_2 m_2}$, and they are related to our $L^{n_3,l_3,m_3}_{n_1,l_1,m_1;n_2,l_2,m_2}$ by the following:

$$L^{n_3,l_3,m_3}_{n_1,l_1,m_1;n_2,l_2,m_2} = \sqrt{\frac{(n_1+1)(n_2+1)}{2\pi^2 (n_3+1)}} C^{n_3 l_3 m_3}_{n_1 l_1 m_1; n_2 l_2 m_2} \tag{B.7}$$

References

Adams, B.L., Henrie, A., Henrie, B., Lyon, M., Kalidindi, S.R., Garmestani, H., 2001. Microstructure-sensitive design of a compliant beam. Journal of the Mechanics and Physics of Solids 49, 1639–1663.

Adams, B.L., Kalidindi, S.R., Fullwood, D.T., 2012. Microstructure-Sensitive Design for Performance Optimization. Butterworth-Heinemann. 1 edition.

Benham, T., 2012. Uniform distribution over a convex polytope.

Bollmann, W., 1984. Triple lines in polycrystalline aggregates as disclinations. Philosophical Magazine A 49, 73–79.

Fast, T., Knezevic, M., Kalidindi, S.R., 2008. Application of microstructure sensitive design to structural components produced from hexagonal polycrystalline metals. Computational Materials Science 43, 374–383.

Frary, M.E., Schuh, C.A., 2005. Connectivity and percolation behaviour of grain boundary networks in three dimensions. Philosophical Magazine 85, 1123–1143.

Hamilton, W.R., 1844. On a new species of imaginary quantities connected with a theory of quaternions. Proceedings of the Royal Irish Academy 2, 424–434.

Hardy, G., Field, D.P., 2011. A triple junction distribution function, in: Materials Science and Technology Conference and Exhibition 2011, MS&T'11, Columbus, OH. pp. 378–384.

Hardy, G., Field, D.P., 2012. Triple Junction Distributions in Grain Boundary Engineered Alloys, in: Materials Science and Technology Conference and Exhibition 2012, MS&T'12, Pittsburgh, PA.

Houskamp, J.R., Proust, G., Kalidindi, S.R., 2007. Integration of Microstructure-Sensitive Design with Finite Element Methods: Elastic-Plastic Case Studies in FCC Polycrystals. International Journal for Multiscale Computational Engineering 5, 261–272.

Jacobson, M., 2012. Representing Polyhedral Convex Hulls by Vertices or (In)Equalities.

Johnson, O.K., Schuh, C.A., 2013. The uncorrelated triple junction distribution function: Towards grain boundary network design. Acta Materialia 61, 2863–2873.

Kalidindi, S.R., Houskamp, J.R., 2007. Application of the Spectral Methods of Microstructure Design to Continuous Fiber-reinforced Composites. Journal of Composite Materials 41, 909–930.

Kalidindi, S.R., Houskamp, J.R., Lyon, M., Adams, B.L., 2004. Microstructure sensitive design of an orthotropic plate subjected to tensile load. International Journal of Plasticity 20, 1561–1575.

Kroese, D.P., Taimre, T., Botev, Z.I., 2011. Handbook of Monte Carlo Methods. Wiley Series in Probability and Statistics, Wiley, Hoboken.

Lehockey, E.M., Limoges, D., Palumbo, G., Sklarchuk, J., Tomantschger, K., Vincze, A., 1999. On improving the corrosion and growth resistance of positive Pb-acid battery grids by grain boundary engineering. Journal of Power Sources 78, 79–83.

Lehockey, E.M., Palumbo, G., 1997. On the creep behaviour of grain boundary engineered nickel. Materials Science and Engineering: A 237, 168–172.

[5]Because Meremianin did not explicitly state the phase convention of what he calls "...the usual 3D-spherical harmonics ..." (Meremianin, 2006), it is possible that there is also a missing factor of $(-1)^l$.

Lehockey, E.M., Palumbo, G., Brennenstuhl, A., Lin, P., 1998a. Mitigating intergranular attack and growth in lead-acid battery electrodes for extended cycle and operating life. Metallurgical and Materials Transactions A 29, 387–396.

Lehockey, E.M., Palumbo, G., Lin, P., 1998b. Improving the weldability and service performance of nickel-and iron-based superalloys by grain boundary engineering. Metallurgical and Materials Transactions A 29, 3069–3079.

Lin, P., Palumbo, G., Erb, U., Aust, K., 1995. Influence of grain boundary character distribution on sensitization and intergranular corrosion of alloy 600. Scripta Metallurgica et Materialia 33, 1387–1392.

Lyon, M., Adams, B.L., 2004. Gradient-based non-linear microstructure design. Journal of the Mechanics and Physics of Solids 52, 2569–2586.

Mason, J.K., 2009. The relationship of the hyperspherical harmonics to SO(3), SO(4) and orientation distribution functions. Acta crystallographica. Section A, Foundations of crystallography 65, 259–66.

Mason, J.K., Schuh, C.A., 2008. Hyperspherical harmonics for the representation of crystallographic texture. Acta Materialia 56, 6141–6155.

MATLAB, 2012. 8.0.0.783 (R2012b). The MathWorks, Inc., Natick, MA.

Meremianin, A.V., 2006. Multipole expansions in four-dimensional hyperspherical harmonics. Journal of Physics A: Mathematical and General 39, 3099–3112.

Morawiec, A., Szpunar, J.A., Hinz, D., 1993. Texture influence on the frequency of occurrence of CSL-boundaries in polycrystalline materials. Acta metallurgica et materialia 41, 2825–2832.

Norton, D.P., Goyal, A., Budai, J.D., Christen, D.K., Kroeger, D.M., Specht, E.D., He, Q., Saffian, B., Paranthaman, M., Klabunde, C.E., Lee, D.F., Sales, B.C., List, F.A., 1996. Epitaxial YBa2Cu3O7 on Biaxially Textured Nickel (001): An Approach to Superconducting Tapes with High Critical Current Density. Science 274, 755–757.

Olson, G.B., 1997. Computational Design of Hierarchically Structured Materials. Science 277, 1237–1242.

Park, S., 2006. Integral evaluation of the linearization coefficients of the product of two Legendre polynomials. JOURNAL OF APPLIED MATHEMATICS AND 20, 623–635.

Patala, S., Mason, J.K., Schuh, C.A., 2012. Improved representations of misorientation information for grain boundary science and engineering. Progress in Materials Science 57, 1383–1425.

Patala, S., Schuh, C.A., 2011. A continuous and one-to-one coloring scheme for misorientations. Acta Materialia 59, 554–562.

Saheli, G., Garmestani, H., Adams, B.L., 2005. Microstructure design of a two phase composite using two-point correlation functions. Journal of Computer-Aided Materials Design 11, 103–115.

Sintay, S.D., Adams, B.L., 2005. Microstructure Design for a Rotating Disk: With Application to Turbine Engines, in: Volume 2: 31st Design Automation Conference, Parts A and B, ASME. pp. 823–834.